Dendritic delay lines shape the computation of sound location in neurons of the gerbil medial superior olive

Authors/affiliations

Jared Casarez[1*], Rebecca I. Voglewede[1*], Bradley D. Winters[2], Ken Ledford[1] and Nace L. Golding[1]

* Equal contributions

The University of Texas at Austin, Department of Neuroscience and Center for Learning and Memory, 1 University Station C7000, Austin TX 78712-0248, USA.

[2]Currently: Department of Biological Sciences and University Hospitals – NEOMED Hearing Research Center, Northeast Ohio Medical University, Rootstown, OH, 44272, United States and Brain Health Research Institute, Kent State University, Kent, OH, 44242, United States

Corresponding author and lead contact

Nace L. Golding: The University of Texas at Austin, Department of Neuroscience and Center for Learning and Memory, 1 University Station C7000, Austin TX 78712-0248, golding@austin.utexas.edu.

Summary

In mammals, neurons of the medial superior olive encode information about sounds arising from discrete spatial locations along the horizon. This tuning requires that an internal delay in the brain must offset acoustic disparities to ensure coincident arrival of excitatory inputs driven from the two ears. The source of this optimal internal delay, originally assumed to arise from axonal delay lines, is currently controversial in mammals. Here we use 2-photon guided paired dendritic and somatic recordings together with compartmental modeling of 40 complete MSO neuron morphologies to demonstrate that the dendrites themselves serve as a significant source of internal delay. We show that most MSO neurons exhibit morphological asymmetries that impose different EPSP delays across dendrites and shifts in optimal interaural time differences. Dendrite-based delays in the mammalian MSO are heterogeneous within each isofrequency laminae and provide a stable, structural mechanism to help tune individual neurons to sounds from different azimuthal locations.

Keywords

dendrite; dendritic filtering; coincidence detection; auditory; sound localization.

Highlights and eTOC blurb

- The dendrites of MSO neurons show graded levels of asymmetry along the medio-lateral axis.
- Dendritic asymmetries impose different cable properties and optimal EPSP timing at the soma

45 • Dendritic asymmetry shifts the location of interaural time difference curves toward
46 electrotonically longer trees
47 • The presence of inhibition does not alter the effects of dendritic asymmetry on ITDs,
48 but helps keep ITDs within the physiological range.

49 Casarez *et al* demonstrate that the bipolar dendritic arbor of mammalian sound localization
50 neurons in the medial superior olive is typically asymmetrical, and that this asymmetry is a
51 critical determinant of the location of spatial tuning curves.

INTRODUCTION

Spatial information in the auditory system is critical for humans and other mammals to assemble a 3-dimensional view of the world as well as to understand speech and communication signals, especially in environments with many sounds overlapping in time and in frequency. The auditory system is distinct from vision or touch in that there is no explicit peripheral representation of space, in this case in the cochlea, only a representation of frequency. Accordingly, the central auditory system must compute horizontal sound location indirectly by combining a series of monaural and binaural cues [1,2]. Spatial coding in the central auditory system is a prime example of a centrally synthesized or computational map.

Interaural time difference cues are used by birds and mammals to compute horizontal sound location at low frequencies [3]. In mammals this computation takes place in the medial superior olive (MSO), whose neurons are the first to receive converging excitatory and inhibitory inputs driven from the two ears. Intriguingly, in individual neurons, binaural inputs are integrated within a bipolar dendritic architecture, with ipsilateral and contralateral excitatory inputs segregated onto lateral and medial dendritic branches respectively [4,5]. Ipsilateral and contralateral inhibition converges onto the soma and proximal dendrites [4–8]. MSO neurons detect the optimal combination of these inputs, converting temporal coincidence into a rate code [6,9,10].

The concept of internal delay is central to coincidence detection in the MSO, where acoustic delays to the two ears are countered in time by a mechanism of delay inside the brain. This internal temporal asymmetry was postulated in early models to arise from

axonal delay lines formed by ladder-like combinations of bilateral excitatory inputs (the "Jeffress model") [11]. While the Jeffress model enjoys strong support in birds [12–14], comparable studies in mammals have failed to reveal systematic axonal input delay lines nor any mapping of delay along the nucleus [6,15,16]. More recently, there is evidence that fast inhibition mediates internal delay by shifting the peaks of EPSPs [17–19]. However, this mechanism is subject to vigorous debate [20–22], and it is not clear that this mechanism alone can explain the range of receptive field locations in the MSO or their insensitivity to sound level. Other mechanisms have been proposed to mediate internal binaural asymmetry, including asymmetrical axon position, medio-lateral differences in the rising slopes of EPSPs [23], and differences in tuning of binaural inputs ("stereausis") [24,25].

All models of coincidence detection must address the issue of the temporal distortions imposed by the dendrites themselves. However, to date models of MSO neurons have been represented either as point neurons or as simplified, symmetrical "ball-and-stick" models [17,26–30]. Previous measurements of dendritic propagation have revealed that EPSPs encounter delays in their propagation to the soma up to ~150 μs, despite some degree of temporal compensation by activation of low voltage-activated K channels in the soma and proximal dendrites [27]. However, these measurements have largely been restricted to the proximal half of the dendritic arbor and have relied on averaging highly variable populations of neurons. Given that the dendrites of MSO neurons alter their branching pattern and diameters during early hearing and following disruptions of normal hearing [31–33], they might serve as a potential mechanism for adjusting the timing requirements for sounds from the two ears to arrive coincidently at the soma and axon.

Here we demonstrate that the dendritic arbors of MSO neurons are highly heterogeneous and show a striking continuum of asymmetry across the medial and lateral branches that receive segregated inputs driven respectively from the two ears. We show with dual 2-photon fluorescence-guided patch recordings that inputs to smaller and/or more distal dendrites show more substantial propagation delays than previously recognized, and computational modeling of a large population of intact neuronal morphologies shows that these dendritic asymmetries translate into stable internal delays that, as a population, could account for the full range of naturally occurring horizontal locations. Finally, we show that inhibition preserves the effects of dendritic asymmetry on interaural time differences (ITDs) and helps bring the region of maximum slope of firing changes within the ecologically relevant range. Thus dendrite-based delay lines likely work synergistically with other integrative mechanisms purported to shape the perception of horizontal position in mammals.

RESULTS

To understand how MSO neurons process interaural time differences in the dendrites, we made fluorescence-guided dendritic and somatic patch-clamp recordings visualized under 2-photon microscopy. Using this approach, we were able to target the distal third of the dendritic arbor, including secondary and tertiary branches, regions that have largely escaped investigation in these neurons. We then injected simulated EPSCs (τ_{rise} and τ_{decay}, 0.2 ms) into the dendritic pipette and recorded potentials simultaneously at both dendrites and soma. We observed strong variability in both the percent amplitude attenuation at the soma $\left(\left(\frac{V_{soma}}{V_{dend}}\right) \times 100\right)$ as well as the propagation delay of the EPSP, measured as the difference in EPSP peak time at the soma relative to the dendrite

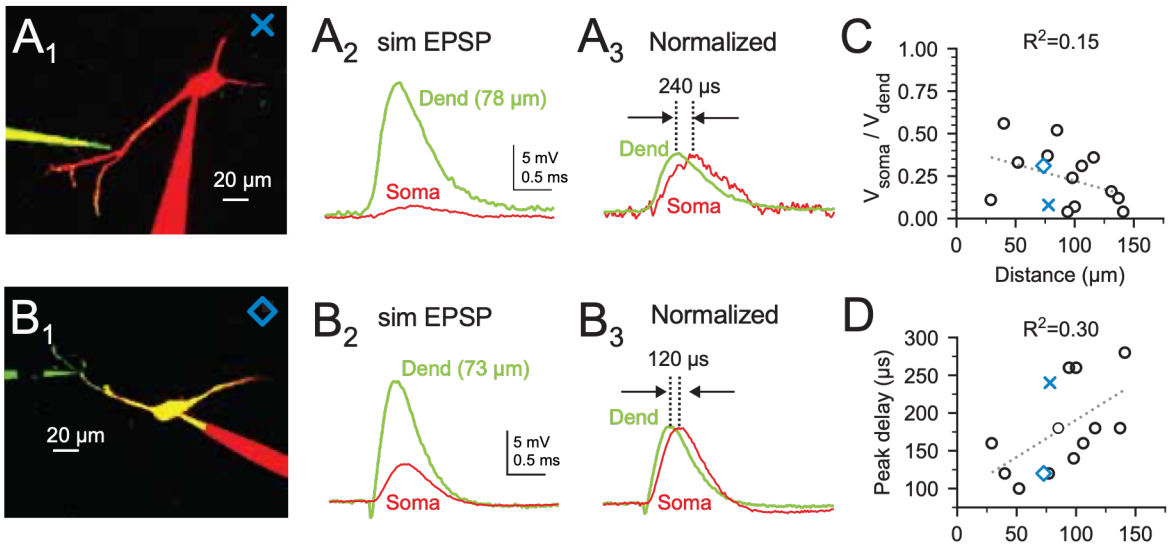

Figure. 1: Heterogeneity in attenuation and timing of simulated excitatory synaptic potentials following propagation from distal dendritic locations to the soma. A,B: 2-photon fluorescence-guided dual dendritic and somatic patch recordings from two MSO neurons of comparable distances (78 and 73 µm, respectively). Example neuron in A1 shows stronger attenuation of somatic propagation of a simulated EPSP (A2 vs B2) and longer peak delay (A3 vs. B3). EPSC amplitudes: cell A, 600 pA; cell B, 400 pA. C,D. Group data for attenuation and peak delay for all paired MSO neuron recordings. There is a poor correlation of both measures as a function of distance.

(Fig. 1). Notably, the delays measured in these recordings ranged between 100 and 300 µs, exceeding the physiological range of ITDs measured in gerbils. In these recordings,

there was little correlation between local morphological features of recorded dendrites and propagation delay of the EPSP, measured as the difference in the peak timing of dendritic and somatic EPSPs (Fig. 2A-C). However, there was a stronger correlation between the local dendritic membrane time constant and EPSP propagation delay (Fig.

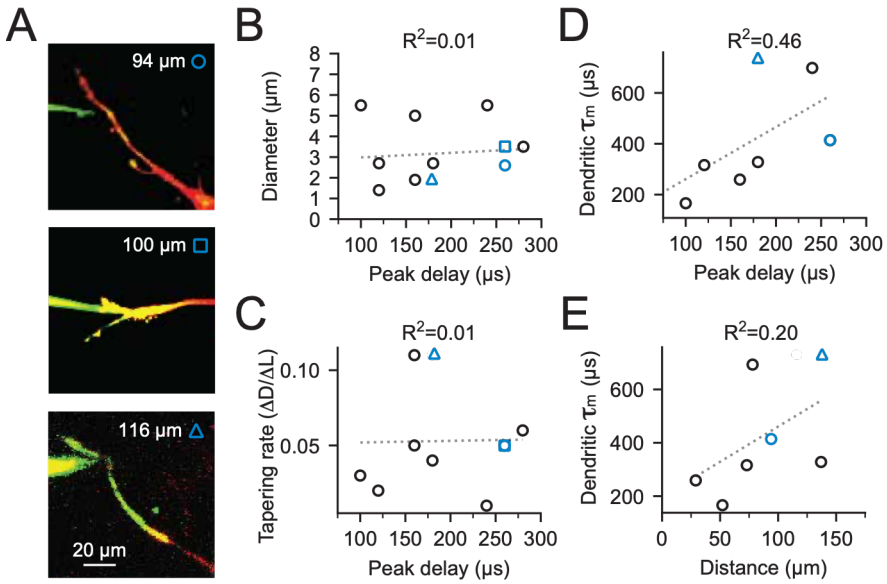

Figure 2: EPSP propagation delays are not correlated with local morphology but rather more global physiological properties. A: Closeups of distal dendritic morphology during paired dendritic and somatic recordings. B,C: Delay of peak EPSPs during propagation from dendrite to soma shows no significant correlation with local diameter or tapering rate of local dendrite. (dendritic EPSCs: 400-1000 pA). D: Peak EPSP delay from dendrite to soma was weakly correlated with the membrane time constant recorded at the dendritic recording site. E: Dendritic membrane time constant increased with distance of the recording site from the soma.

2D). In addition, there was a weak trend of increasing dendritic membrane time constant with recording distance (Fig. 2E), possibly because of proximity to the dendritic terminations. These results may reflect that an understanding of the integrative properties of the dendrites requires an analysis of the larger morphological and electrotonic structure of the neuron.

To understand how overall dendritic structure impacts binaural coincidence detection, we analyzed a database of biocytin-filled MSO neurons that exhibited complete dendritic structures (40 of 270 neurons from Bondy et al., 2021 [34] ; Fig. 3). We quantified dendritic length, surface area and branching, with special emphasis on comparisons of medial and lateral dendritic arbors. Higher-order (2° and higher) dendritic branches were prominent in these neurons, comprising 70% of the membrane surface area (Fig. S1).

137 A striking feature of most neurons in this data set was an overall asymmetry between the
138 lateral and medial dendritic arbors, reflecting differences in length, branching, and/or
139 diameter of the dendrites (Fig. 3A-C). We quantified this asymmetry according to two

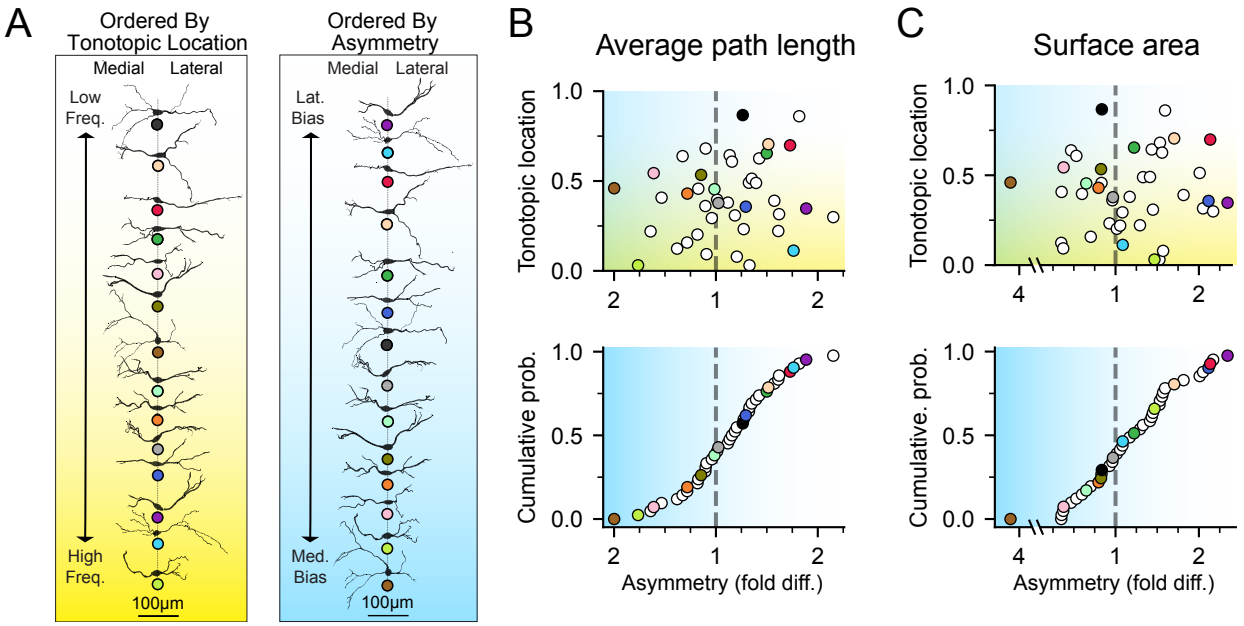

Figure 3: MSO neuron morphology is inhomogeneous and asymmetric, regardless of tonotopy. A: Reconstructed morphologies rank ordered by tonotopy (left) and degree of asymmetry (right). Orderings span from low frequency (top) to high frequency (bottom) and lateral (top) and medial (bottom) asymmetry, respectively. Colored gradients added to visualize ordering. Uniquely colored dots placed beneath each morphology for differentiation. B: Fold difference between average path length of medial and lateral dendrites for all reconstructed morphologies with vertical axes ordered by tonotopic location (top) or degree of asymmetry (bottom). Gradients added as in A. Colored points correspond to A. C: Same as B, except comparing total surface area of medial and lateral branches. Average medio-lateral path length and surface area fold differences (± SEM) were 1.080 ± 0.057 and 1.112 ± 0.133 (biased laterally) and tonotopic R^2 values were -0.42 and -0.23.

140 parameters, the average path length (average length from each dendritic end to the
141 soma) and membrane surface area, with the latter parameter reflecting the collective
142 influence of dendritic length, diameter and branching pattern. We then defined the degree
143 of bilateral asymmetry as fold differences between the larger vs. smaller dendritic
144 measure for each parameter. We observed no obvious correlation between dendritic
145 asymmetry and tonotopic location (Fig. 3A, *left* and 3B, *top*). However, we found that
146 dendritic asymmetry formed a finely graded continuum, with a slight bias toward lateral
147 dendrites (Fig. 3B, *bottom*). Interestingly, there were no significant differences in

population averages of the medio-lateral path length and surface area (1.080 ± 0.057 and 1.112 ± 0.133 fold differences; p=0.562), though there was a slight lateral bias. These results indicate that the averaging of dendritic morphological parameters across neurons obscures what is likely a key structural and computational feature.

To understand how morphological asymmetry impacts synaptic integration, we constructed compartmental models using the same 40 reconstructions analyzed in Fig. 3. We introduced an excitatory synaptic conductance (alpha function: τ = 290 µs) into each dendritic compartment and then measured the voltage attenuation and propagation delay from the dendritic input location to the soma (Figs. 4-5). At comparable distances from the soma, EPSP amplitude at the site of synaptic input and following propagation to the

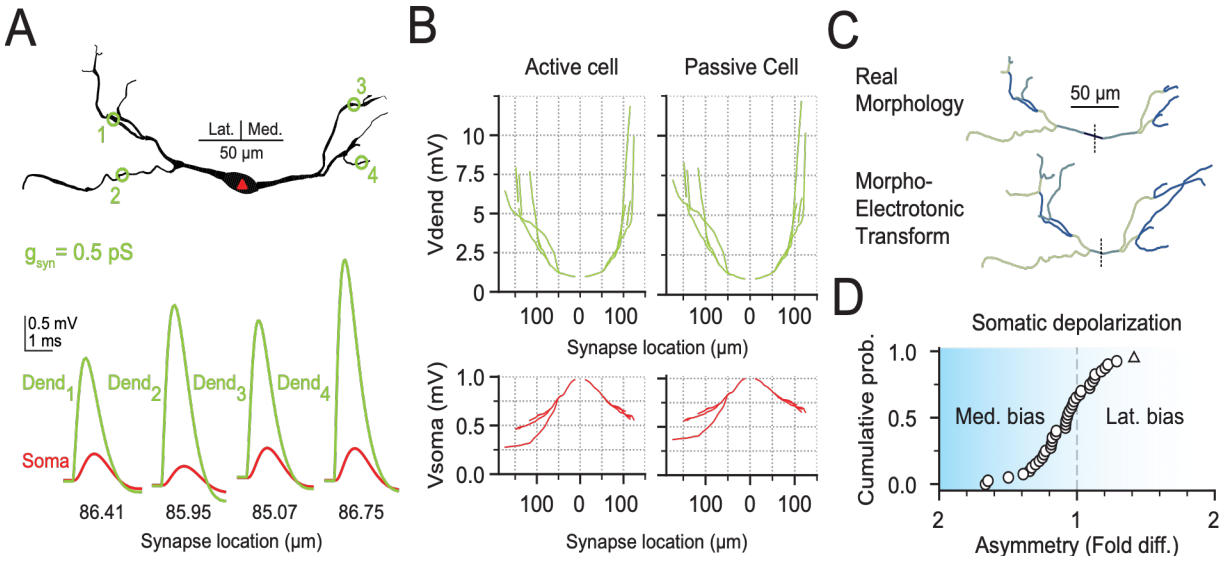

Figure 4: MSO morphology nonlinearly filters and attenuates propagating EPSPs through its passive cable properties. A: Visualization EPSP filtering at different dendritic sites. Cell morphology (top) with similarly distant example synaptic sites indicated with green circles and corresponding numbers. Red triangle indicates the somatic compartment. Synaptic conductance indicated as g_{syn}. Four sets of paired dendritic (green) and somatic (red) traces (bottom) for each example synaptic site. Numbering of traces corresponds to labels on morphology above. Dendritic distance from soma for each site indicated below traces. B: Same procedure as in A, with an adjusted unitary synaptic conductance (see Methods), with measurements from each computational compartment. Model morphology and orientation same as in A. Comparison between active channel (left) and passive channel model (right). Recorded EPSP amplitude at synaptic (top, green) and somatic (bottom, red) compartment as a function of distance from soma. C: Actual (top) and electrotonically transformed (bottom) morphologies. Transformation visualizes degree of EPSP attenuation from each compartment (see Methods). D: Group data (n=40) of average somatic depolarization asymmetry between mediolateral sides. Gradient as in Fig 3. Dotted line indicates equal medial and lateral average somatic depolarizations. Cell from A-C indicated with a triangle.

158 soma varied considerably, like the physiological data from paired recordings in Figure 1
159 (Fig. 4A). Plots of local dendritic and propagated somatic EPSP amplitudes across all
160 synapse locations further revealed striking asymmetries in propagation efficacy of EPSPs
161 to the soma (Fig. 4B, “Active cell”). In MSO neurons, the timing and attenuation of EPSPs
162 along dendrites are influenced both by passive cable filtering as well as interactions with
163 low voltage-activated K channels, which are active in the subthreshold voltage range in
164 these neurons [27] . To determine the degree to which asymmetries in low voltage-activated
165 K channels impact EPSP attenuation at the soma we converted all voltage-activated
166 conductances to leak channels (Fig. 4B, “Passive cell”; see Methods). While EPSPs
167 propagated slightly more effectively to the soma from all dendritic locations in the passive
168 model, it did not fundamentally disrupt mediolateral asymmetry, indicating that these
169 differences arose primarily from the passive electrotonic architecture of the cell. The
170 branching structure had a significant effect on dendritic propagation asymmetry. This
171 could be better visualized in inward morphoelectrotonic transforms of cells, which exhibits
172 dendritic compartments according to their electrotonic, versus physical lengths. In the
173 example neuron in Fig. 4C, large primary dendrites are deemphasized, while thinner
174 secondary and tertiary branches appear as electrotonically elongated. Differences
175 between the medial and lateral dendritic arbors in this neuron and many others gave rise
176 to asymmetries in the magnitude of the average EPSP arriving at the soma.

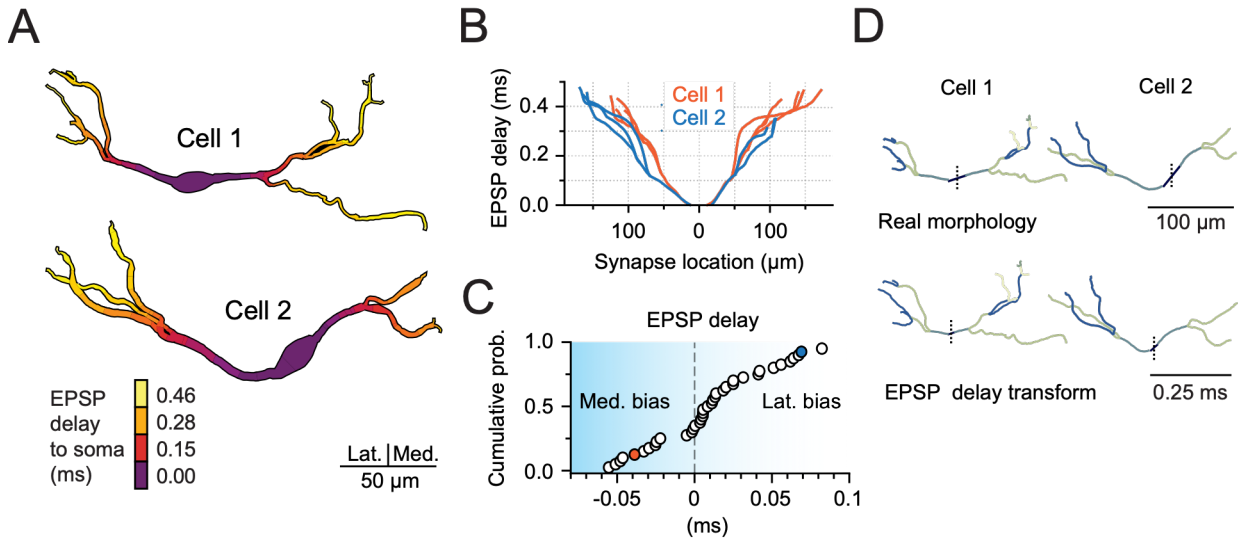

Figure 5: EPSP timing significantly varies within and between cells, with morphological asymmetry informing overall cell timing. A: EPSP delay visualization in two exemplar MSO neurons. Coloring of each cell corresponds to the propagation delay of EPSPs to the soma from its respective compartment. Legend of propagation delay coloring in top right. Cells are oriented mediolaterally according to the scale bar. Outline added to increase gradient readability. B: Same data as in A, except as a function of distance from the soma. Orientation of cells same as in A. C: Group data (n=40) of the difference in average EPSP propagation delay between medial and lateral dendrites. Cells 1 & 2 are indicated with same color as in B. Dotted line at 0 ms indicates an equal average EPSP delay between sides. Blue gradient along horizontal axis (as in Fig. 3) to indicate spectrum of asymmetry. D: Morphological transforms according to EPSP delays. Morphological centroids of actual cell morphologies (top) and transformed morphologies (bottom). Length corresponds to each sections EPSP delay contribution. Coloring of cell sections is consistent between actual and transformed morphologies for easier differentiation and comparison. Dotted line added to mark the midline.

177 Further, we observed that our population of cells formed a continuum in the degree of
178 somatic depolarization asymmetry, in line with the asymmetry in dendritic structure (Fig.
179 4D). Dendritic asymmetry also translated into differences in average EPSP timing across
180 the medial and lateral dendrites. Figure 5A shows for two example neurons the spatial
181 profile of delays of EPSPs propagating from each dendritic compartment to the soma.
182 The asymmetry in dendritic timing can be more quantitatively visualized in plots of peak
183 EPSP delay ($t_{dend} – t_{soma}$) as a function of dendritic distance from the soma (Fig. 5B).
184 Dendritic branch points often introduced substantial jumps in propagation delays, and this
185 is reflected in these plots as increases in slope. To quantify the influence of dendritic
186 asymmetry on the optimal summation of bilateral EPSPs at the soma, we measured the
187 electrotonic delay at the soma for every 2 µm compartment of lateral and medial dendritic

188 subtrees. In our population of 40 neuron models, there were differences in the average
189 relative time of arrival of EPSPs to the soma from compartments in the medial and lateral
190 dendrites. Further, these differences formed a smoothly graded continuum of delays
191 (Fig. 5C).

192 MSO neurons exhibit a range of intrinsic electrical properties, and so we examined a
193 subset of neuron morphologies to understand the functional implications of this
194 physiological diversity. Using a neuron with an asymmetric dendritic arbor, we
195 systematically slowed the membrane time constant by reducing the density of both low
196 voltage-activated K channels and HCN channels (Fig. S2). In both cases, the timing of
197 EPSPs reaching the soma was linearly related to the value of the membrane time
198 constant. Thus, the effects of dendritic asymmetry on EPSP timing and amplitude at the
199 soma are expected to be substantially higher in MSO neurons with slower intrinsic
200 membrane properties. To understand how the differential timing of EPSPs propagating
201 from medial and lateral dendrites is translated into ITDs, we simulated binaural excitatory
202 input using a spiking model of MSO neurons (see Methods). This model featured one
203 axonal input per terminal branch segment as well as a centripetal (dendrite-to-soma)
204 pattern of dendritic innervation, running from the terminal compartments to the soma, in
205 accordance with results from anatomical studies (Fig. 6A) [15,16,28]. The conduction velocity
206 of these inputs was set to 1 ms^{-1}, approximating values of unmyelinated terminal axonal
207 arborizations of similar caliber [13,35] . The timing of ipsilateral and contralateral inputs was
208 varied systematically, triggering spiking only when the two inputs were in close
209 coincidence (Fig. 6B). The location of these excitatory ITD functions were dependent on
210 medio-lateral asymmetry. Functions shifted toward the side of the electrically longer

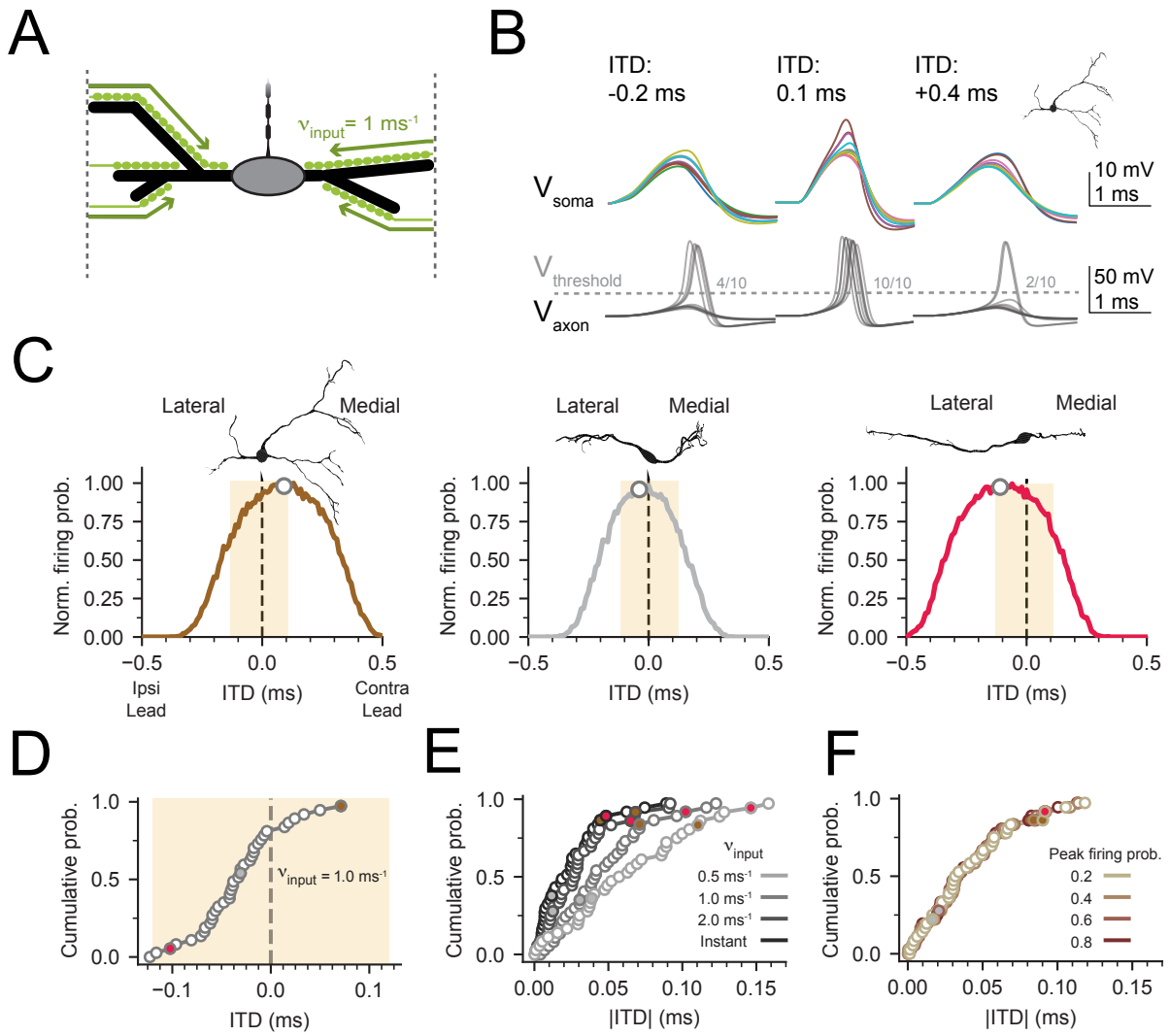

Figure 6: Simulated ITDs demonstrate conservation of morphological impact on coincident detection. A: Schematic visualization of ITD innervation. Somatic compartment and dendrites are shown in gray and black, respectively. Green bulbs represent excitatory synapses, with corresponding arrows to illustrate axonal input velocity (v_{input}). Dotted lines illustrate point at which there is considered to be no axonal input delay. Axon attached to soma, with initial segment, nodes, and internodes. B: Example somatic (top) and axonal (bottom) traces from ITD simulations. ITDs of -0.2 ms (left), 0.1 ms (middle, optimal coincidence), 0.3 ms (right) shown. Traces colored only for differentiation. Dotted line ($V_{threshold}$) indicates depolarization threshold for action potential consideration. Morphology of model cell indicated in upper right. C: Three example ITD firing curves from varied morphologies, medially biased (left), symmetrical (middle), and laterally biased (right). Corresponding morphologies imaged above. Light orange span represents range of ecologically possible ITDs for model species. Dashed line placed at ITD of 0 ms. Dot indicates centroid ITD value. D: Sorted group data (n=39) of centroid ITDs, with v_{input} = 1 ms^{-1}. Cells from C indicated with filled colored points. E-F: Sorted group data (n=39) of absolute centroid ITDs, varying axonal input velocity (E) and peak firing probability (F). Cells from C indicated with correspondingly filled colored points.

211 dendrite, reflecting the need for earlier activation of that side to compensate for a longer

212 dendritic propagation delay (Fig. 6C). Our population of 40 neurons showed peak firing

213 at delays that traversed a continuum of values (-0.11 to 0.08 ms, median -0.02; Fig. 6D;

214 Fig. S3). The precise range of values depended in part on the assumptions on the velocity
215 of excitatory axons. The largest range of ITDs was achieved when there was closer
216 matching between the velocity of axonal input velocity and postsynaptic EPSPs
217 propagating from the dendrites to the soma, which maximized temporal coincidence at
218 the soma of spatially disparate inputs in the dendrites (Fig. 6E). Finally, ITDs shifted less
219 than 3% in the face of input amplitude changes that resulted in firing probabilities between
220 0.2 and 0.8, indicating that dendritic asymmetry is highly stable across changing stimulus
221 conditions.

222 Inhibition is a critical component of ITD encoding, although its precise role is subject to
223 vigorous debate. To understand how dendritic asymmetry impacts the effects of inhibition,
224 we added bilateral inhibitory conductances to the somatic compartment of the bilateral
225 excitatory model in Fig. 6, consistent with the known somatically biased innervation of
226 MSO neurons from the lateral and medial nuclei of the trapezoid body (LNTB and
227 MNTB; [8,36]). We set the timing of inhibitory conductances to be 500 μs in advance of
228 excitatory inputs from the same side, in accordance with a previously published
229 estimate [21] . We then adjusted the amplitude of inhibitory conductances to produce
230 summed IPSPs of between ~1-3 mV, which reduced firing probability by 20, 40, 60 and
231 100% (Fig. 7A). With increasing amplitude of IPSPs, resultant ITD functions decreased
232 in halfwidth by 57%, but the location of functions with increasing levels of inhibition were
233 not significantly different from the model with only excitatory inputs (0.070-0.078 ms;

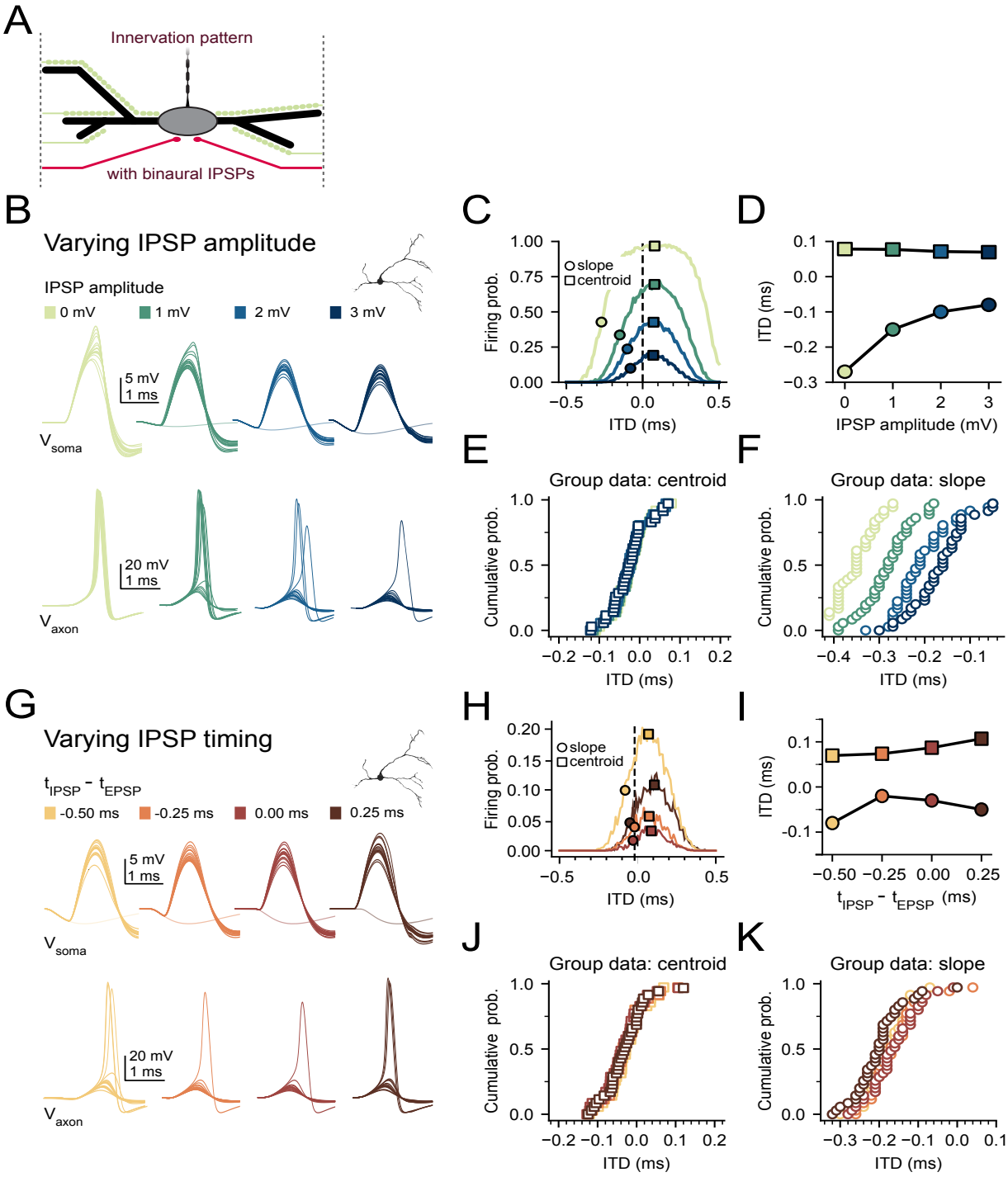

Figure 7: Inhibition may serve to modulate a pre-established morphological baseline ITD response. A: Schematic of innervation pattern with excitatory (green) and inhibitory (red) inputs. B: Somatic (top) and axonal (bottom) traces from ITD stimulation (ITD: 0.1 ms; IPSP timing: -0.5 ms) for each tested IPSP amplitude. Tested amplitude values and their unique colors above corresponding traces. Morphology of the exemplar neuron shown in the upper right. C: Exemplar cell's ITD response curves colored corresponding to IPSP amplitude in B. Centroid (square) and maximum slope (circle) are indicated for each curve. Dotted line at an ITD of zero. D: ITD centroid and maximum slope as a function of IPSP amplitude (colors corresponding to B). E-F: Group data (n=39) for ITD centroids (E) and steepest sections (F) for each IPSP amplitude. Data in E are largely overlapping. Shifting of population data in F corresponds to trend seen in the exemplar cell (D). G-K: Same as B-F, instead varying the timing of the inhibition (IPSP amplitude: 3 mV). Absolute firing probability, in H, is lower than C, resulting in lower signal to noise ratio. Centroids in I show more variation than D, though still minimal. Shift of exemplar cell's maximum slope ITD section (I) corresponds to degree of reduction in absolute firing probability (H).

234 centroid, p=0.984; group data). However, the region of maximum slope consistently

shifted towards zero, in accordance with a sinking iceberg receptive field scenario (Fig. 7D; -0.27 to 0.07 ms). We then tested how the relative timing of excitatory and inhibitory inputs altered ITD functions. Varying the timing of IPSPs relative to EPSPs from –0.5 ms to 0.25 ms altered the location of ITD functions by 0.04 ms, from 0.07 to 0.11 ms. Over the population of MSO neuron morphologies, the presence of inhibition reduced firing probability without fundamentally shifting the location of ITD functions. However, the region of the function where there is maximal change in firing rate is necessarily impacted by the decrease in ITD width (Fig. S4), suggesting that dendritic asymmetry and inhibition provide separate contributions to MSO neurons' receptive field locations.

DISCUSSION

The passive cable properties of neuronal dendrites are known to impart both attenuation and delay on EPSPs as they propagate to the soma, commensurate with the distance traversed and the anatomical features of the dendrite itself. However, the functional significance of dendritic geometry and its impact on action potential firing is often difficult to assess. Here we have newly identified a critical function for dendritic structure in the processing of sound localization cues in MSO neurons of the auditory brainstem. We have shown that the bipolar dendritic arbor of MSO neurons is typically asymmetrical, imposing a corresponding asymmetry in the relative timing required for excitatory inputs to drive optimal patterns of action potential output. Our compartmental models show that variation in dendritic morphology across cells exerts a continuum of temporal influences sufficient to shift spatial receptive fields across the full biological range of ITDs available to the gerbil. These shifts are insensitive to differences in intensity and likely work together with other sources of internal delay to enable MSO neurons to stably encode spatial locations along the horizontal plane.

Role of dendritic-based delays in the detection of input sequences

The idea that dendritic structure could dictate detection of temporal sequences of input was first explored in the pioneering computer models of Wilfred Rall. These studies showed that attenuation and propagation delays of EPSPs traveling from the dendrites to the soma could impart greater sensitivity to somatically vs distally directed activation sequences of excitatory inputs, where the longer propagation time of more distal EPSPs is compensated by their earlier activation [37] . Preferential firing to centripetal (distal to

267 proximal) temporal sequences of uncaged glutamate at spines has been demonstrated
268 in cortical neurons in slices, but it is not clear what natural conditions would generate such
269 sequences [38]. By contrast, single excitatory axonal inputs to MSO dendrites mediate a
270 natural centripetal sequence of synaptic activity [15,28,39] , and both current and previous
271 modeling results highlight the importance of matching of input sequence conduction
272 velocity with that of MSO dendrites, which conduct EPSPs at an average of ~0.3 ms^{-1}. In
273 the present study, with the aid of 2-photon fluorescence-guided recordings we have been
274 able to sample smaller diameter secondary and tertiary dendrites at longer distances from
275 the soma. Our results reveal that the attenuation and delays of EPSPs propagating from
276 these processes to the soma are more severe than previously estimated [40] . In our sample
277 of modeled MSO neurons, these slower-conducting non-primary dendrites make up 70%
278 of the surface area of the dendritic arbor in our sample of MSO neurons and thus play an
279 outsized role in exerting temporal shifts in ITD curves in neurons with asymmetrical
280 dendritic trees. These results emphasize that both branching and dendritic diameter are
281 critical determinants of dendritic delay, as seen reflected in the morphoelectrotonic
282 transforms (Fig. 5).

283 In the visual system, asymmetrical length and branching of the dendrites drives temporal
284 disparities in the pattern of inhibition of ganglion cells, providing directional tuning to
285 object movement [41–43]. The computation in the auditory system differs from vision in
286 several fundamental ways. In the retina, spatial information is directly represented at the
287 level of the photoreceptors, and tuning to spatial movement relies on the relative arrival
288 times of excitatory and inhibitory inputs to the dendrites and soma. By contrast, in the
289 cochlea space is not explicitly represented on the basilar membrane, which decomposes

290 complex sounds spatially into different frequency channels. Accordingly, horizontal spatial
291 receptive fields must be constructed *de novo* in the MSO through the detection of synaptic
292 binaural coincidence. In this way, ITDs serve as a proxy for horizontal position.

293 *Other sources of asymmetry in binaural coincidence detection*

294 Although our data reveal that the dendrites may contribute significant interaural delays in
295 the binaural circuitry in the MSO, they likely work together with other mechanisms that
296 have been proposed to influence binaural coincidence detection. In ~25% of MSO
297 neurons in gerbils, the axon emerges from either the lateral or medial dendrites [44,45] , and
298 these results appear to extend to other mammalian species, including guinea pigs and
299 cats [46,47] . Results from computer models suggest these offset axons, like asymmetrical
300 dendrites, introduce strong asymmetries in synaptic integration and ITD tuning [48] .

301 Inhibition has received considerable attention as a mechanism for ITD tuning based on
302 shifts of tuning curves measured in single-unit recordings *in vivo* upon iontophoretic block
303 of glycinergic synapses [18,19] . However, these results are controversial, as strong
304 inhibition has not been observed in both juxtacellular and intracellular patch recordings *in*
305 *vivo* [20,21,49], and there have been concerns about iontophoretic strychnine having off-
306 target effects that that alter both firing probability and input resistance [20]. We found that
307 inhibition did not shift the overall location of ITD curves across the functional range of
308 IPSP magnitudes *(*Fig. 7), consistent with pressure-applied strychnine data *in vivo* [20].
309 Inhibition shifted the location of maximal change in firing rate, consistent with a
310 conventional "iceberg" model of inhibitory action on neuronal receptive fields. In
311 mammals, the maximum rate of change, or slope of ITDs may be more important for

312 population encoding of ITDs. Given that the maximal rising slope of firing invariably shifts
313 toward 0 μs ITD when inhibition narrows ITD curves, both inhibition and dendritic
314 asymmetry would both play key roles in setting the location of individual MSO neurons'
315 receptive fields.

316 *Comparison with avian binaural coincidence detectors.*

317 Binaural coincidence detection has been extensively studied in birds, and thus the
318 comparison to mammals is noteworthy. Unlike mammals, dendritic morphology in bird
319 MSO (nucleus laminaris) shows striking dependence on tonotopic location, exhibiting
320 longer, more highly branched dendrites in neurons from low frequency regions [33,50]. While
321 these tonotopic differences in dendritic length have garnered considerable attention, a
322 close examination of dendritic parameters shows that nucleus laminaris neurons, like
323 those in mammalian MSO, exhibit a continuum of dendritic asymmetry in the length of
324 dendrites receiving ipsilateral and contralateral inputs (Smith and Rubel 1979, their Fig.
325 15 [33]). In these low frequency regions, inputs are restricted to distal, higher order
326 branches [51]. Based on both our electrophysiological and modeling data, these higher
327 order branches incur the largest delays as compared to the large-caliber primary
328 dendrites and thus would be the primary determinants of dendritic propagation delay on
329 each side. In the more highly specialized barn owls, the dendrites of laminaris neurons
330 are more limited, and thus internal delay compensation must lie squarely on those
331 provided by unmyelinated afferents [13] .

332 *Dendritic morphology and the scaling problem across species.*

333 The biological range of ITDs varies with head size [52,53], and thus any mechanism of
334 internal delay must be scalable across species, accounting for ITDs differing by hundreds
335 of microseconds (e.g., gerbil: ±130 μs [54], human: ± 600-700 μs [55]). A dendrite-based
336 source of internal delay would be easily scalable, as the length of MSO dendrites
337 increases with the size of different species. Although quantitative data are not available,
338 previous morphological studies in guinea pig, ferret, cat and humans show that the
339 dendritic arbors show considerable asymmetries [46,47,56,57].

340

341 **METHODS**

342 All procedures were conducted in agreement with the Institutional Animal Care and Use
343 Committee at The University of Texas at Austin (UT-Austin), which followed the guidelines
344 of the National Institutes of Health. Mongolian gerbils (*Meriones unguiculatus*) were
345 housed and raised in a colony at the UT-Austin Animal Resource Center. Animals
346 experienced a 50/50 day/night cycle and had continuous access to food and water.

347 *Brain slice preparation*: both male and female gerbils (17-40 days old) were anesthetized
348 with isoflurane and decapitated upon loss of the choroid reflex. The brain was removed
349 from the cranium under warm (34-35°C) artificial cerebrospinal fluid (ACSF), the
350 cerebellum was removed and the isolated hindbrain was glued to the stage of an
351 oscillating tissue slicer (Leica VT-1200S). Horizontal sections were prepared at 200 μm
352 thickness and stored at 35°C in a holding chamber for 45-60 min., and then gradually
353 cooled to room temperature (24°C). All solutions were continuously bubbled with
354 95% O_2 / 5% CO_2. ACSF contained (in mM): 125 mM NaCl, 25 mM D-glucose, 2.5 mM

355 KCl, 25 mM $NaHCO_3$, 1.25 mM NaH_2PO_4, 1.5mM $MgSO_4$, 1.5 mM $CaCl_2$, pH adjusted to
356 7.45 with NaOH, and final osmolarity at 315 mOsm.

357 *Imaging and electrophysiological acquisition and analyses:* neurons in the MSO were
358 visualized under gradient contrast optics on a Leica TCS SP5 System equipped with a
359 Coherent Chameleon Ultra II Ti:sapphire laser and an 8 kHz resonant scanner under
360 control of Leica LAS AF Imaging Software. We found that gradient contrast images
361 acquired via the photomultiplier tubes were of poor contrast in the heavily myelinated
362 regions of the auditory brainstem, and so cell selection and seal formation was carried
363 out under gradient contrast imaging through the epifluorescence port of the microscope
364 and detected on a high-resolution monochrome digital camera (Zeiss Axiocam 503)
365 running Zen software. The soma was recorded in whole-cell current clamp mode with a
366 pipette (4 to 8 MΩ resistance) containing a potassium gluconate-based solution with 40-
367 80 μM Alexa 594 added for visualizing cell morphology. After waiting ~10 min. for the dye
368 to fill the dendritic arbor, a dendritic recording was made under 2-photon fluorescence
369 with a second pipette (8 to 15 MΩ resistance) containing the same K Gluconate solution
370 with 40-80 μM Alexa 488. Pipette solutions had a composition of 115 mM K-gluconate,
371 4.42 mM KCl, 0.5 mM EGTA, 10 mM HEPES, 10 mM, Na_2Phosphocreatine, 4 mM MgATP,
372 and 0.3 mM NaGTP. Osmolality was adjusted to 300 mOsm/L with sucrose, and pH was
373 adjusted to 7.30 with KOH. Seal resistances exceeded 1 GΩ, and recordings were
374 discontinued if series resistances exceeded 20 or 50 MΩ for somatic and dendritic
375 recordings, respectively.
376 Electrophysiological recordings were under the control of custom routines written in
377 IGOR-Pro (Wavemetrics). Pipettes were prepared on a Sutter P-1000 puller using

378 borosilicate glass (1.5 mm O.D.). Data was acquired using a pair of Dagan BVC-700,
379 amplifiers in conjunction with an ITC-18 computer interface (Heka Instruments). Data was
380 low-pass filtered at 5 kHz, sampled at 50 kHz, and stored on a Macintosh computer for
381 further analyses using custom-written routines in IGOR-Pro.

382 *Compartment model construction:*

383 A subpopulation of 40 fully intact reconstructed MSO neurons was selected from those
384 gathered in Bondy et al. (2021) [34] . The reconstructed morphologies were imported into
385 the NEURON simulation environment, using its Neurolucida importing tool.
386 Computational compartments were created every 2 μm (Fig. S5A). Somatic and dendritic
387 compartments were applied channel kinetics differentially, consisting of low and high-
388 voltage-activated K channels [27,58] , HCN channels[59] , and leak channels, with sodium
389 channels[60] exclusively in the somatic compartments. In simulations modeling a passive
390 cell, high and low-voltage potassium and HCN channels were replaced with passive leak
391 channels with conductances set to the average resting conductance of the preexisting
392 active channels. In simulations with an axon, a model axon, with morphology as in
393 Lehnert (2014) [61] , was attached at the center of the model soma. The axon channel
394 kinetics implemented consisted of sodium channels, low-threshold potassium channels
395 and leak channels in the nodes and initial segments, with solely leak channels in the
396 internodes. Measurements from the axon were all recorded from the fifth node. Simulated
397 synapses were conductance-based and shaped by an alpha function (τ = 290 μs).

398

Channel	Dendrite	Soma	TAIS	CAIS	Internode	Node
KLT (Mathews, 2010)	20	40	155	155		155
KHT (Nabel, 2019)	0.55	0.55				
HCN (Khurana, 2011)	1	1	2	2		
Na (Scott, 2010)	0	30	250	250		250
Leak	0.05	0.05	0.05	0.05	0.02	5

Table 1: Maximal channel conductances (μS/cm^2). Tapered axon initial segment (TAIS) and constant disameter axon initial segment (CAIS).

399 *Simulation variations:* When measuring EPSP propagation, synapses were placed every
400 2 μm, with a unitary conductance that would maximally depolarize the soma 1 mV (unless
401 noted otherwise). Each synapse was then stimulated and recorded separately. In ITD
402 coincident detection procedures, dendrites were innervated with synapses (release
403 probability=0.45) placed every 2 μm, totaling ~125 synapses for each side [62] . To mimic
404 axonal activation, an artificial axonal input delay (Δt_{axon}) was calculated for each synapse
405 as a function of conduction velocity (ν_{input}) and axonal travel distance. The travel distance
406 was considered zero at each side's furthest point from the soma. Otherwise, the axonal
407 travel distance consists of two components: the mediolateral distance from the furthest
408 point (Δt_{axon}=0) to the synapse's closest terminal segment; the path length from that
409 terminal segment to the synapse (Fig. S5B). Artificial ITDs could then be added onto the
410 calculated axonal delay. Each artificial ITD value (-0.5 to 0.5 ms, incremented by 0.01),
411 was tested with 400 trials, and each trial consisted of a single stimulation of all synapses.
412 To provide a more binary output, a model axon was attached to the cell's soma, and a

spike was reported if a 25 mV depolarization from rest was recorded at the fifth and final axonal node. The synapses could then be adjusted with a unitary conductance to achieve an acceptable maximum firing probability. When implementing IPSP inputs to the ITD procedure, two inhibitory synapses were added at the soma, one corresponding to each mediolateral side. Each synapse generated an IPSP shaped by an alpha function with a time constant of 1.5 ms [62]. The timing of the synapses was adjusted relative to the artificial excitatory ITD signals. The amplitude of the IPSPs was adjusted by modifying the inhibitory synapses' conductances to achieve a combined IPSP hyperpolarization of approximately 1, 2, and 3 mV.

Data analyses

Measures of dendritic distance, both in slice experiments and in compartment models, were taken as the length along the dendritic arbor to the center of the somatic compartment. To address the variable size of the MSO within the slice plane, a normalized tonotopic location was calculated as the cell's distance from the most dorsal point of the MSO, relative to the entire MSO dorsoventral length. To provide a quantitative value of asymmetry between each cell's morphological measures, a unit of fold difference $\left(\log_2\left(\frac{\max\{\text{medial},\ \text{lateral}\}}{\min\{\text{medial},\ \text{lateral}\}}\right)+1\right)$ was used, with a value of 1 and 2 representing equal and double values, respectively. Average path length measurements were taken from the distances along the dendrite to the soma from each terminal section of the corresponding mediolateral arbor. Measurements for propagation attenuation and timing were taken at both the synaptic and somatic compartments of the model cell. For attenuation, the somatic depolarization for mediolateral sides was calculated by averaging each synaptic

compartments propagated EPSP amplitude at the soma. Morpho-electrotonic transforms were created by scaling each sections length according to the natural logarithm of its attenuation $\left(\text{section length} = \ln\left(\frac{V_{dend}}{V_{soma}}\right)\right)$. EPSP delay values were calculated by measuring the time between peak depolarization in the synaptic and somatic compartments. The corresponding delay transforms are scaled according to the delay contribution of each section. Mediolateral comparisons of delay were calculated by subtracting each sides average EPSP delay for all compartments. To minimize noise and data filtering for the ITD response, the centroid of the curve was measured, where half of the total area under the curve exists on either side. Comparisons were made using the absolute ITD centroid values to highlight the population of neurons' collective change. The ITD firing probabilities were smoothed with a Savitzky–Golay filter for the purpose of reasonably identifying the region of max slope for the curves.

448 **REFERENCES**

449

450 1. Grothe, B., and Pecka, M. (2014). The natural history of sound localization in
451 mammals--a story of neuronal inhibition. Front Neural Circuits *8*, 116.
452 https://doi.org/10.3389/fncir.2014.00116.

453 2. Joris, P., and Yin, T.C. (2007). A matter of time: internal delays in binaural
454 processing. Trends Neurosci *30*, 70–78. https://doi.org/10.1016/j.tins.2006.12.004.

455 3. Carr, C.E., Soares, D., Parameshwaran, S., and Perney, T. (2001). Evolution and
456 development of time coding systems. Current Opinion in Neurobiology *11*, 727–733.
457 https://doi.org/10.1016/s0959-4388(01)00276-8.

458 4. Stotler, W.A. (1953). An experimental study of the cells and connections of the
459 superior olivary complex of the cat. J Comp Neurol *98*, 401–431.

460 5. Lindsey, B.G. (1975). Fine structure and distribution of axon terminals from the
461 cochlear nucleus on neurons in the medial superior olivary nucleus of the cat. J Comp
462 Neurol *160*, 81–103. https://doi.org/10.1002/cne.901600106.

463 6. Yin, T.C., and Chan, J.C. (1990). Interaural time sensitivity in medial superior olive of
464 cat. J Neurophysiol *64*, 465–488.

465 7. Magnusson, A.K., Kapfer, C., Grothe, B., and Koch, U. (2005). Maturation of
466 glycinergic inhibition in the gerbil medial superior olive after hearing onset. J Physiol
467 *568*, 497–512. https://doi.org/10.1113/jphysiol.2005.094763.

468 8. Kapfer, C., Seidl, A.H., Schweizer, H., and Grothe, B. (2002). Experience-dependent
469 refinement of inhibitory inputs to auditory coincidence-detector neurons. Nat Neurosci *5*,
470 247–253. https://doi.org/10.1038/nn810.

471 9. Spitzer, M.W., and Semple, M.N. (1995). Neurons sensitive to interaural phase
472 disparity in gerbil superior olive: diverse monaural and temporal response properties. J
473 Neurophysiol *73*, 1668–1690.

474 10. Goldberg, J.M., and Brown, P.B. (1969). Response of binaural neurons of dog
475 superior olivary complex to dichotic tonal stimuli: some physiological mechanisms of
476 sound localization. J Neurophysiol *32*, 613–636.

477 11. Jeffress, L.A. (1948). A place theory of sound localization. J Comp Physiol Psychol
478 *41*, 35–39.

479 12. Carr, C.E., and Konishi, M. (1988). Axonal delay lines for time measurement in the
480 owl's brainstem. Proc Natl Acad Sci U S A *85*, 8311–8315.

481 13. Carr, C., and Konishi, M. (1990). A circuit for detection of interaural time differences
482 in the brain stem of the barn owl.

483 14. Moiseff, A., and Konishi, M. (1981). Neuronal and behavioral sensitivity to binaural
484 time differences in the owl. J Neurosci *1*, 40–48. https://doi.org/10.1523/jneurosci.01-01-
485 00040.1981.

486 15. Beckius, G.E., Batra, R., and Oliver, D.L. (1999). Axons from anteroventral cochlear
487 nucleus that terminate in medial superior olive of cat: observations related to delay
488 lines. J Neurosci *19*, 3146–3161.

489 16. Smith, P.H., Joris, P.X., Carney, L.H., and Yin, T.C. (1991). Projections of
490 physiologically characterized globular bushy cell axons from the cochlear nucleus of the
491 cat. J Comp Neurol *304*, 387–407. https://doi.org/10.1002/cne.903040305.

492 17. Myoga, M.H., Lehnert, S., Leibold, C., Felmy, F., and Grothe, B. (2014). Glycinergic
493 inhibition tunes coincidence detection in the auditory brainstem. Nat Commun *5*, 3790.
494 https://doi.org/10.1038/ncomms4790.

495 18. Pecka, M., Brand, A., Behrend, O., and Grothe, B. (2008). Interaural time difference
496 processing in the mammalian medial superior olive: the role of glycinergic inhibition. J
497 Neurosci *28*, 6914–6925. https://doi.org/10.1523/jneurosci.1660-08.2008.

498 19. Brand, A., Behrend, O., Marquardt, T., McAlpine, D., and Grothe, B. (2002). Precise
499 inhibition is essential for microsecond interaural time difference coding. Nature *417*,
500 543–547. https://doi.org/10.1038/417543a.

501 20. Franken, T.P., Roberts, M.T., Wei, L., Golding, N.L., and Joris, P.X. (2015). In vivo
502 coincidence detection in mammalian sound localization generates phase delays. Nat
503 Neurosci *18*, 444–452. https://doi.org/10.1038/nn.3948.

504 21. Roberts, M.T., Seeman, S.C., and Golding, N.L. (2013). A mechanistic
505 understanding of the role of feedforward inhibition in the mammalian sound localization
506 circuitry. Neuron *78*, 923–935. https://doi.org/10.1016/j.neuron.2013.04.022.

507 22. Heijden, M. van der, Lorteije, J.A., Plauska, A., Roberts, M.T., Golding, N.L., and
508 Borst, J.G. (2013). Directional hearing by linear summation of binaural inputs at the
509 medial superior olive. Neuron *78*, 936–948.
510 https://doi.org/10.1016/j.neuron.2013.04.028.

511 23. Jercog, P.E., Svirskis, G., Kotak, V.C., Sanes, D.H., and Rinzel, J. (2010).
512 Asymmetric excitatory synaptic dynamics underlie interaural time difference processing
513 in the auditory system. PLoS Biol *8*, e1000406.
514 https://doi.org/10.1371/journal.pbio.1000406.

24. Shamma, S.A., Shen, N., and Gopalaswamy, P. (1989). Stereausis: binaural processing without neural delays. The Journal of the Acoustical Society of America *86*, 989–1006. https://doi.org/10.1121/1.398734.

25. Plauška, A., Heijden, M.V.D., and Borst, J.G.G. (2017). A test of the stereausis hypothesis for sound localization in mammals. Journal of Neuroscience *37*, 7278–7289. https://doi.org/10.1523/jneurosci.0233-17.2017.

26. Agmon-Snir, H., Carr, C.E., and Rinzel, J. (1998). The role of dendrites in auditory coincidence detection. Nature *393*, 268–272. https://doi.org/10.1038/30505.

27. Mathews, P.J., Jercog, P.E., Rinzel, J., Scott, L.L., and Golding, N.L. (2010). Control of submillisecond synaptic timing in binaural coincidence detectors by K(v)1 channels. Nat Neurosci *13*, 601–609. https://doi.org/10.1038/nn.2530.

28. Callan, A.R., Hess, M., Felmy, F., and Leibold, C. (2021). Arrangement of Excitatory Synaptic Inputs on Dendrites of the Medial Superior Olive. J Neurosci *41*, 269–283. https://doi.org/10.1523/jneurosci.1055-20.2020.

29. Franken, T.P., Bremen, P., and Joris, P.X. (2014). Coincidence detection in the medial superior olive: Mechanistic implications of an analysis of input spiking patterns. Frontiers in Neural Circuits *8*, 42. https://doi.org/10.3389/fncir.2014.00042.

30. Dasika, V.K., White, J.A., and Colburn, H.S. (2007). Simple models show the general advantages of dendrites in coincidence detection. J Neurophysiol *97*, 3449–3459. https://doi.org/10.1152/jn.00669.2005.

31. Feng, A.S., and Rogowski, B.A. (1980). Effects of monaural and binaural occlusion on the morphology of neurons in the medial superior olivary nucleus of the rat. Brain Research *189*, 530–534. https://doi.org/10.1016/0006-8993(80)90112-2.

32. Russell, F.A., and Moore, D.R. (1999). Effects of unilateral cochlear removal on dendrites in the gerbil medial superior olivary nucleus. Eur J Neurosci *11*, 1379–1390.

33. Smith, D.J., and Rubel, E.W. (1979). Organization and development of brain stem auditory nuclei of the chicken: dendritic gradients in nucleus laminaris. J Comp Neurol *186*, 213–239. https://doi.org/10.1002/cne.901860207.

34. Bondy, B.J., Haimes, D.B., and Golding, N.L. (2021). Physiological diversity influences detection of stimulus envelope and fine structure in neurons of the medial superior olive. J Neurosci. https://doi.org/10.1523/jneurosci.2354-20.2021.

35. Hoffmeister, B., Jänig, W., and Lisney, S.J.W. (1991). A proposed relationship between circumference and conduction velocity of unmyelinated axons from normal and regenerated cat hindlimb cutaneous nerves. Neuroscience *42*, 603–611. https://doi.org/10.1016/0306-4522(91)90402-a.

550 36. Werthat, F., Alexandrova, O., Grothe, B., and Koch, U. (2008). Experience-
551 dependent refinement of the inhibitory axons projecting to the medial superior olive. Dev
552 Neurobiol *68*, 1454–1462. https://doi.org/10.1002/dneu.20660.

553 37. Rinzel, J., and Rall, W. (1974). Transient response in a dendritic neuron model for
554 current injected at one branch. Biophys J *14*, 759–790. https://doi.org/10.1016/s0006-
555 3495(74)85948-5.

556 38. Branco, T., Clark, B.A., and Häusser, M. (2010). Dendritic discrimination of temporal
557 input sequences in cortical neurons. Science *329*, 1671–1675.
558 https://doi.org/10.1126/science.1189664.

559 39. Smith, P.H., Joris, P.X., and Yin, T.C. (1993). Projections of physiologically
560 characterized spherical bushy cell axons from the cochlear nucleus of the cat: evidence
561 for delay lines to the medial superior olive. J Comp Neurol *331*, 245–260.
562 https://doi.org/10.1002/cne.903310208.

563 40. Winters, B.D., Jin, S.X., Ledford, K.R., and Golding, N.L. (2017). Amplitude
564 Normalization of Dendritic EPSPs at the Soma of Binaural Coincidence Detector
565 Neurons of the Medial Superior Olive. J Neurosci *37*, 3138–3149.
566 https://doi.org/10.1523/jneurosci.3110-16.2017.

567 41. Bloomfield, S.A. (1994). Orientation-sensitive amacrine and ganglion cells in the
568 rabbit retina. Journal of Neurophysiology *71*, 1672–1691.
569 https://doi.org/10.1152/jn.1994.71.5.1672.

570 42. Trenholm, S., Johnson, K., Li, X., Smith, R.G., and Awatramani, G.B. (2011).
571 Parallel mechanisms encode direction in the retina. Neuron *71*, 683–694.
572 https://doi.org/10.1016/j.neuron.2011.06.020.

573 43. Bloomfield, S.A. (1991). Two types of orientation-sensitive responses of amacrine
574 cells in the mammalian retina. Nature *350*, 347–350. https://doi.org/10.1038/350347a0.

575 44. Scott, L.L., Mathews, P.J., and Golding, N.L. (2005). Posthearing developmental
576 refinement of temporal processing in principal neurons of the medial superior olive. J
577 Neurosci *25*, 7887–7895. https://doi.org/10.1523/jneurosci.1016-05.2005.

578 45. Rautenberg, P.L., Grothe, B., and Felmy, F. (2009). Quantification of the three-
579 dimensional morphology of coincidence detector neurons in the medial superior olive of
580 gerbils during late postnatal development. J Comp Neurol *517*, 385–396.
581 https://doi.org/10.1002/cne.22166.

582 46. Cajal., S.R.Y. (1907). Structure et connexions des neurones. Nordiskt Medicinskt
583 Arkiv *40*, 1–28. https://doi.org/10.1111/j.0954-6820.1907.tb00034.x.

47. Smith, P.H. (1995). Structural and functional differences distinguish principal from nonprincipal cells in the guinea pig MSO slice. J. Neurophysiol. *73*, 1653–1667. https://doi.org/10.1152/jn.1995.73.4.1653.

48. Zhou, Y., Carney, L.H., and Colburn, H.S. (2005). A model for interaural time difference sensitivity in the medial superior olive: interaction of excitatory and inhibitory synaptic inputs, channel dynamics, and cellular morphology. J Neurosci *25*, 3046–3058. https://doi.org/10.1523/jneurosci.3064-04.2005.

49. Plauska, A., Borst, J.G., and Heijden, M. van der (2016). Predicting binaural responses from monaural responses in the gerbil medial superior olive. J Neurophysiol *115*, jn 01146 2015. https://doi.org/10.1152/jn.01146.2015.

50. Wang, Y., and Rubel, E.W. (2008). Rapid regulation of microtubule-associated protein 2 in dendrites of nucleus laminaris of the chick following deprivation of afferent activity. Neuroscience *154*, 381–389. https://doi.org/10.1016/j.neuroscience.2008.02.032.

51. Yamada, R., and Kuba, H. (2021). Dendritic synapse geometry optimizes binaural computation in a sound localization circuit. Science Advances *7*. https://doi.org/10.1126/sciadv.abh0024.

52. Jones, H.G., Koka, K., Thornton, J.L., and Tollin, D.J. (2011). Concurrent development of the head and pinnae and the acoustical cues to sound location in a precocious species, the chinchilla (Chinchilla lanigera). J Assoc Res Otolaryngol *12*, 127–140. https://doi.org/10.1007/s10162-010-0242-3.

53. Koka, K., Jones, H.G., Thornton, J.L., Lupo, J.E., and Tollin, D.J. (2011). Sound pressure transformations by the head and pinnae of the adult Chinchilla (Chinchilla lanigera). Hear Res *272*, 135–147. https://doi.org/10.1016/j.heares.2010.10.007.

54. Maier, J.K., and Klump, G.M. (2006). Resolution in azimuth sound localization in the Mongolian gerbil (Meriones unguiculatus) . The Journal of the Acoustical Society of America *119*, 1029–1036. https://doi.org/10.1121/1.2159429.

55. George, K. (1977). Model for the intramural time differences in the azimuthal plane. J. Acoust. Soc. Am *62*, 157–167.

56. Henkel, C.K., and Brunso-Bechtold, J.K. (1990). Dendritic morphology and development in the ferret medial superior olivary nucleus. J Comp Neurol *294*, 377–388. https://doi.org/10.1002/cne.902940307.

57. Kulesza, R. (2008). Cytoarchitecture of the human superior olivary complex: nuclei of the trapezoid body and posterior tier. Hear Res *241*, 52–63. https://doi.org/10.1016/j.heares.2008.04.010.

58. Nabel, A.L., Callan, A.R., Gleiss, S.A., Kladisios, N., Leibold, C., and Felmy, F. (2019). Distinct distribution patterns of potassium channel sub-units in somato-dendritic compartments of neurons of the medial superior olive. Frontiers in Cellular Neuroscience *13*, 409471. https://doi.org/10.3389/fncel.2019.00038/bibtex.

59. Khurana, S., Liu, Z., Lewis, A.S., Rosa, K., Chetkovich, D., and Golding, N.L. (2012). An essential role for modulation of hyperpolarization-activated current in the development of binaural temporal precision. J Neurosci *32*, 2814–2823. https://doi.org/10.1523/jneurosci.3882-11.2012.

60. Scott, L.L., Mathews, P.J., and Golding, N.L. (2010). Perisomatic voltage-gated sodium channels actively maintain linear synaptic integration in principal neurons of the medial superior olive. J Neurosci *30*, 2039–2050. https://doi.org/10.1523/jneurosci.2385-09.2010.

61. Lehnert, S., Ford, M.C., Alexandrova, O., Hellmundt, F., Felmy, F., Grothe, B., and Leibold, C. (2014). Action potential generation in an anatomically constrained model of medial superior olive axons. J Neurosci *34*, 5370–5384. https://doi.org/10.1523/jneurosci.4038-13.2014.

62. Couchman, K., Grothe, B., and Felmy, F. (2010). Medial superior olivary neurons receive surprisingly few excitatory and inhibitory inputs with balanced strength and short-term dynamics. J Neurosci *30*, 17111–17121. https://doi.org/10.1523/jneurosci.1760-10.2010.